Received: 29 August 2021 | Revised: 21 October 2021 | Accepted: 22 October 2021

DOI: 10.1002/amp2.10107

RESEARCH ARTICLE

JOURNAL OF ADVANCED MANUFACTURING AND PROCESSING WILEY

4D printing of thermal responsive structure for environmentally adaptive radiative cooling and heating

Yuchen Liu[1] | **Ruochen Liu**[2] | **Jingjing Qiu**[3] | **Shiren Wang**[1,2]

[1]Department of Industrial and Systems Engineering, Texas A&M University, College Station, Texas, USA

[2]Department of Materials Science and Engineering, Texas A&M University, College Station, Texas, USA

[3]Department of Mechanical Engineering, Texas Tech University, Lubbock, Texas, USA

Correspondence
Shiren Wang, Department of Industrial and Systems Engineering, Texas A&M University, College Station, TX 77843, USA.
Email: s.wang@tamu.edu

Funding information
Texas A&M; National Science Foundation

Abstract

Four-dimensional (4D) printing, which combines a three-dimensional (3D) printing process with dynamic modulation of materials, provides a possible solution to achieve stimuli-responsive microstructure that exhibit more complex functionality. One of the potential applications for these stimuli-responsive hydrogels is switchable passive radiative cooling and warming. However, most current attempts are limited to mono-functionality, either radiative cooling or warming only. In this article, we demonstrate a double-side morphing flower structure for a dual functionality, switchable cooling or warming dependent on the environment. The morphing structure was designed with the aid of emissivity calculations and then fabricated by the 3D printing method. The transition between open-flower and close-flower states occurs at 32°C within a minute, resulting in ~35% emissivity difference between these two states. As a result, the power difference between inner layer and outer layer was as high as 22 W/m^2 which is a function of pyramid bottom size.

KEYWORDS

4D printing, environmentally adaptive, radiative cooling, radiative heating

1 | INTRODUCTION

Stimuli-responsive microstructures are a significant solutions to passive adaptive systems.[1] Specifically, hydrogels are widely used to change swelling behavior and volume in response to surrounding stimuli such as pH, ionic strength, temperature, magnetic field, and light.[2] One of the potential applications for these stimuli-responsive hydrogels is the switchable passive radiative cooling and heating.

According to the observation of land surface temperature (LST) over the United States, the diurnal temperature range (DTR) can be as high as 25°C or more in summer and 15°C or more in winter over 50% of the area of the US.[3] The yearly mean DTR of the US is about 13.5°C.[4] The rolling changes between cold and hot temperature in a short period require an automatically switchable thermal management strategy to provide a comfortable environment in a building in order to reduce energy consumption and foster global sustainability. The rapid temperature changes between day and night not only cause significant consumption of energy and greenhouse gas emissions but also has a significant impact on human health. Therefore, an environmentally adaptive sustainable strategy is urgently needed to automatically implement radiative cooling functionality in hot weather and radiative heating at cold ambient temperatures, as well as a quick switch between radiative cooling and radiative heating functions to fit different situations. By now, many artificial structures have achieved monofunctional radiative cooling, including layered structure-based membrane,[5–8] microparticle filling-based membrane,[9,10] and patterned structure-based membrane.[11–14] However, these technologies cannot respond to environmental changes and lack an effective mechanism to regulate heating and cooling dual-functionally. Progress for dual-functional structures is very limited. Zhang et al.[15] designed a dynamic gating of IR radiation through the opening and closing of a bundle of yarn, but it shows the same IR transmittance on both sides of the membrane,

resulting in low efficiency of heating and cooling even though it is switchable. Hsu et al.[16] demonstrated a dual-mode device with electrostatically controlled thermal contact conductance with high cooling and heating power. However, this design is limited to the roof of buildings since it requires a roller system to change the heating and cooling film. Despite much effort to design radiative cooling and heating structures by fabricating static membranes or by replacing the cover directly, none of them can achieve environmentally adaptive radiative cooling and heating in response to the ambient temperature.

Four-dimensional (4D) printing combines three-dimensional (3D) printing process with dynamic modulation of materials. It provides a possible solution to achieve stimuli-responsive microstructure that exhibit more complex functionality. Two-photon polymerization (2PP) is the simplest method of multi-photon lithography (MPL) which can improve the fabrication process of 3D structures in 4D printing.[17] Due to the optical nonlinearity of two-photon absorption, the polymerization process of photoresist is confined at a focal volume (ellipsoidal voxels) with high spatial resolution (<200 nm). However, the feasibility of achieving stimuli-responsive materials with adaptive structure is not clear. The relationship between the 4D printing process and the corresponding stimuli–response should be addressed, and the functionality of the designed structure needs to be investigated.

In this article, we designed and fabricated a thermal responsive structure for environmentally adaptive cooling and heating and term it an environmentally adaptive

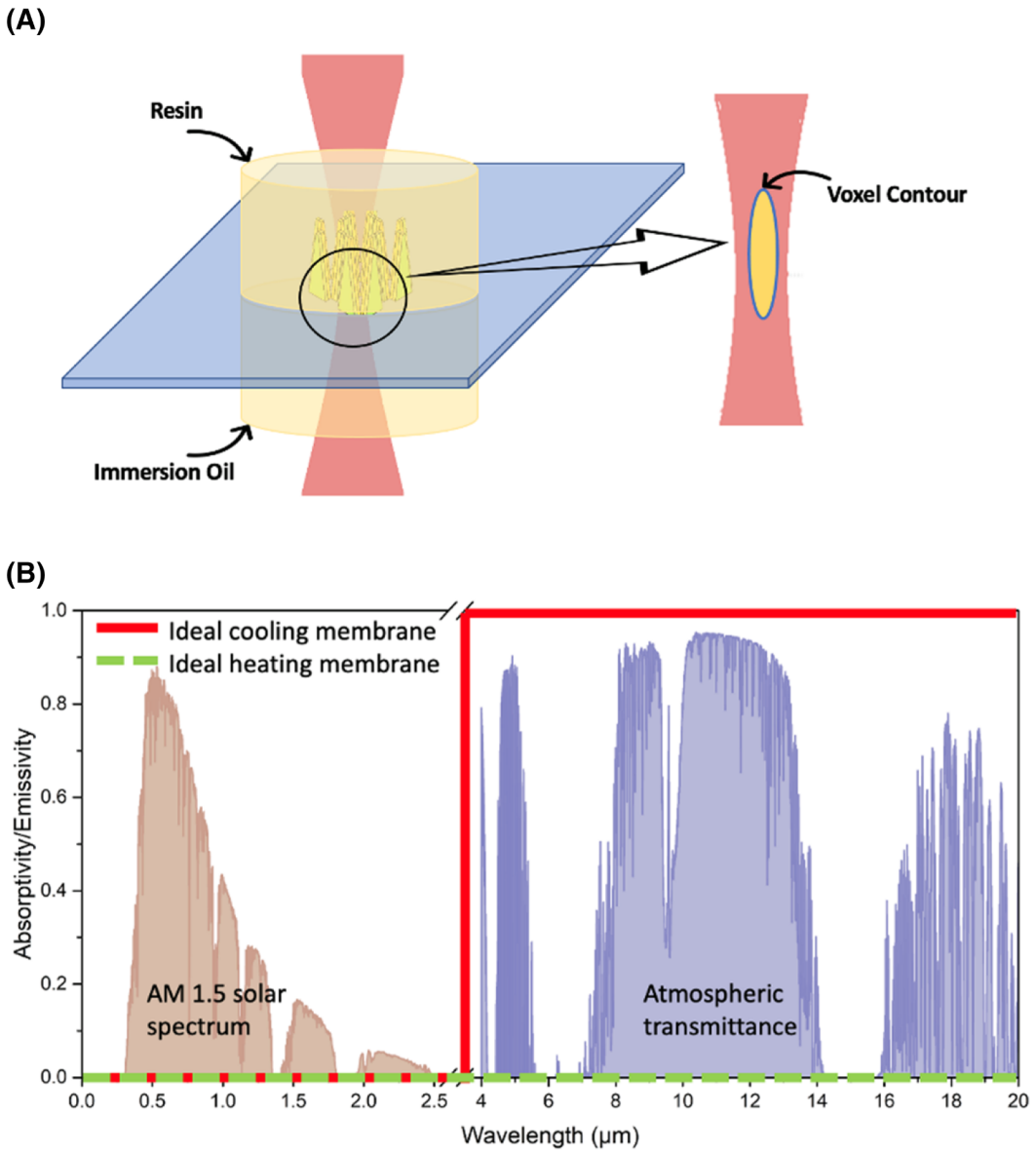

FIGURE 1 (A) Schematic of two-photon polymerization (2PP) for PNIPAM microstructure fabrication. (B) Absorption/emission spectra of two ideal membranes. AM 1.5 solar spectrum (shaded brown). The atmospheric transmittance $t(\lambda)$ is plotted in shaded purple

membrane (EAM). To achieve environmentally adaptive radiative cooling and heating to support global sustainability, the surface of materials should be "smart." The surface should change its function (either radiative cooling or radiative heating) in response to the ambient temperature. Poly(N-isopropylacrylamide) (PNIPAM) is an exceptional thermal responsive polymer and seems a perfect candidate for this application.[18] PNIPAM exhibits in a highly swollen state as the ambient temperature below its lower critical solution temperature (LCST) of ~32°C.[19] When the temperature is higher than the LCST, the polymer expels water and forms a dehydrated state. 2PP technology (shown in Figure 1(A)) was used to fabricate the as-designed structure at the resolution of 1-μm. The control of the printing parameters and the printability of the designed structures was investigated. The radiative cooling and heating capability and adaption of as-fabricated systems were characterized. The absorption/emission spectra of ideal cooling and heating membrane is shown in Figure 1(B). The AM 1.5 solar spectrum and atmospheric window are also plotted for reference.[20,21]

2 | STRUCTURE DESIGN AND NUMERICAL SIMULATION

In order to achieve environmentally adaptive radiative cooling and heating, the material structure that responds to the environmental temperature change is critical. A pyramid structure, which looks like a closed flower, has a promising selectivity of mid-infrared absorption to realize high-performance radiative cooling.[13,14] To achieve environmentally radiative cooling and warming in a single emitter material, the emitter should be switchable between high absorptivity and low absorptivity. The closed-flower structure could effectively reflect the IR radiation and reduce the transmittance, resulting in radiative cooling capability. In contrast, the open-flower structure cannot realize this function. The double-layered system can be designed based on this knowledge, as shown in Figure 2 (A). When the ambient temperature is low, the membrane exhibits the heating function. The shape of the outside layer is the open-flower condition, which allows the atmospheric radiation to come through for heating the zone covered by the membrane. The inside closed-flower structure can effectively prevent heat loss. When the ambient temperature is high, the membrane can realize the cooling function. The outside structures are automatically transformed to the closed-flower condition to prevent the atmospheric radiation from passing through. The inside structures change to the open-flower state, respectively, allowing the inside heat to get out in the form of IR radiation. The detailed mechanism is illustrated in Figure 2(B).

As shown in Figure 2, the closed-flower structure will allow trapping the IR radiation while the open-flower structure will let IR radiation pass through. The transformation between the closed-flower and open-flower formats will automatically allow self-cooling and heating in response to the environment. The relationship between the structure and the corresponding emissivity on the atmospheric window and solar spectrum was investigated to guide the structure design and material selection. The critical issue for radiative cooling is reducing the absorbance from the environment and increasing the emissivity from inside to outside. Similarly, for radiative heating, the essential factor is reducing the emissivity from the inside object. Simulation of the emissivity of different structures and resulting cooling or heating function provides insight into the design of the responsive material structure. The numerical simulations were carried out using the finite element (FE) method and the finite-difference time-domain (FDTD) approaches based on Maxwell's Equations and Planck's Law. Since the closed-flower structure looks like a pyramid with a platform on the top, we could design a pyramid structure representing the closed-flower structure and four triangular prisms to define the open-flower structure. Since the pyramid structure shows the extraordinary emissivity in the range of the atmospheric window,[13] several dimensional factors need to be studied. First of all, the vertex angle of a pyramid structure is the most significant factor, determining the reflection of electromagnetic waves amongst the pyramids. Generally, the reflection rate increases as the vertex angle decreases, and the IR radiation, as a kind of electromagnetic wave, will be reflected more and absorbed less.[22] On the other hand, as the vertex angle decreases, more pyramid structures and higher height are needed to cover a given area. Herein, we position the vertex angle of the pyramid (denoted at θ) at 15° to balance the conflict between size and reflectivity.[22] Ideally, the tip of the pyramid structure is a point, but it is extremely difficult to fabricate. Usually, a platform at the top of the pyramid is created in the fabrication process. Accordingly, the pyramid structure with a small platform, including the geometrical parameters, is designed for numerical simulation, as shown in Figure 3 (A, B). The bottom length, top length, gap distance of the structure, and height are denoted as a, b, c, and h, respectively. All the parameters are designed for the closed-flower system. The open-flower structures are calculated according to the closed-flower structure. In the numerical simulation, the refractive index of the designed structure was assumed to 1.50 for PNIPAM based on the literature.[23] As shown in Figure 3(C, D), when the gap distance (denoted as c) is constant, the valley of the absorptivity shifts towards the atmospheric window range as the geometric parameters (a, b, and h) increase. Specifically, when

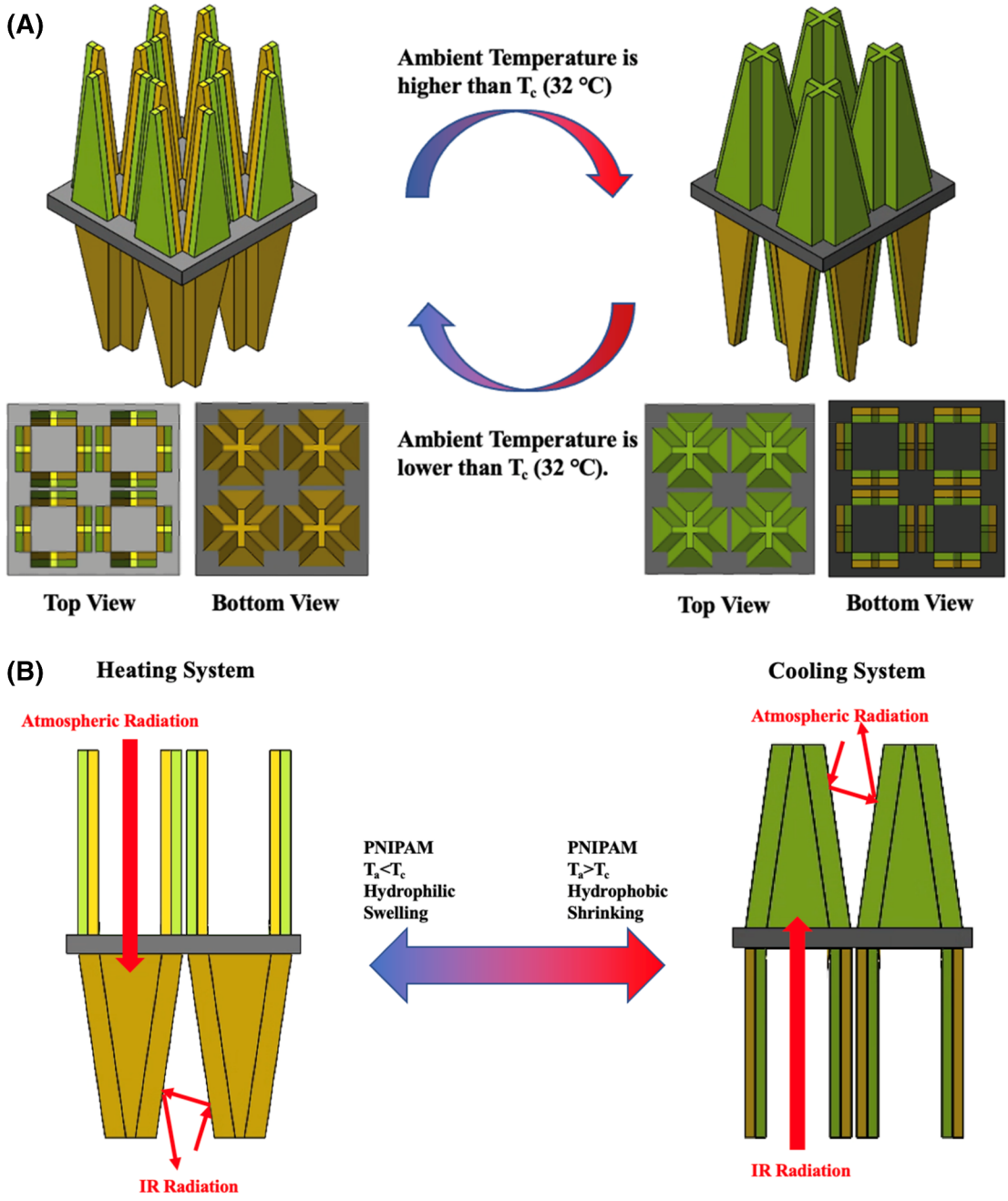

FIGURE 2 Schematic of responsive structure for environmentally adaptive cooling and warming. (A) Environmental temperature-induced structure evolution for radiative cooling and heating. (B) the mechanism of environmentally adaptive self-cooling and heating membrane through IR radiation transmission and reflection

the bottom length of the pyramid structure is greater than 30 μm, the valley of the absorptivity will be located in the atmospheric window. Therefore, the optimal bottom size of the pyramid structure would be 30 μm. On the other hand, as shown in Figure 3(E, F), when the bottom width is a constant, the absorptivity decreases as the gap distance (*c*) increases. To optimize the absorptivity, it is better to make the gap distance as small as possible. However, considering the feasibility of the printing process, the gap distance should match the resolution of the 3D printer.

3 | TWO-PHOTON LASER LITHOGRAPHY OF PNIPAM MICROSTRUCTURES

The fabrication of the EAM structures has been demonstrated using the 2PP method. To maintain the stability of the 3D design, the ratio between the monomer (here N-isopropylacrylamide (NIPAM)) and the crosslinker (here N,N′-methylenebis(acrylamide) (Mbis)) is critical. A high concentration of crosslinkers helps to construct

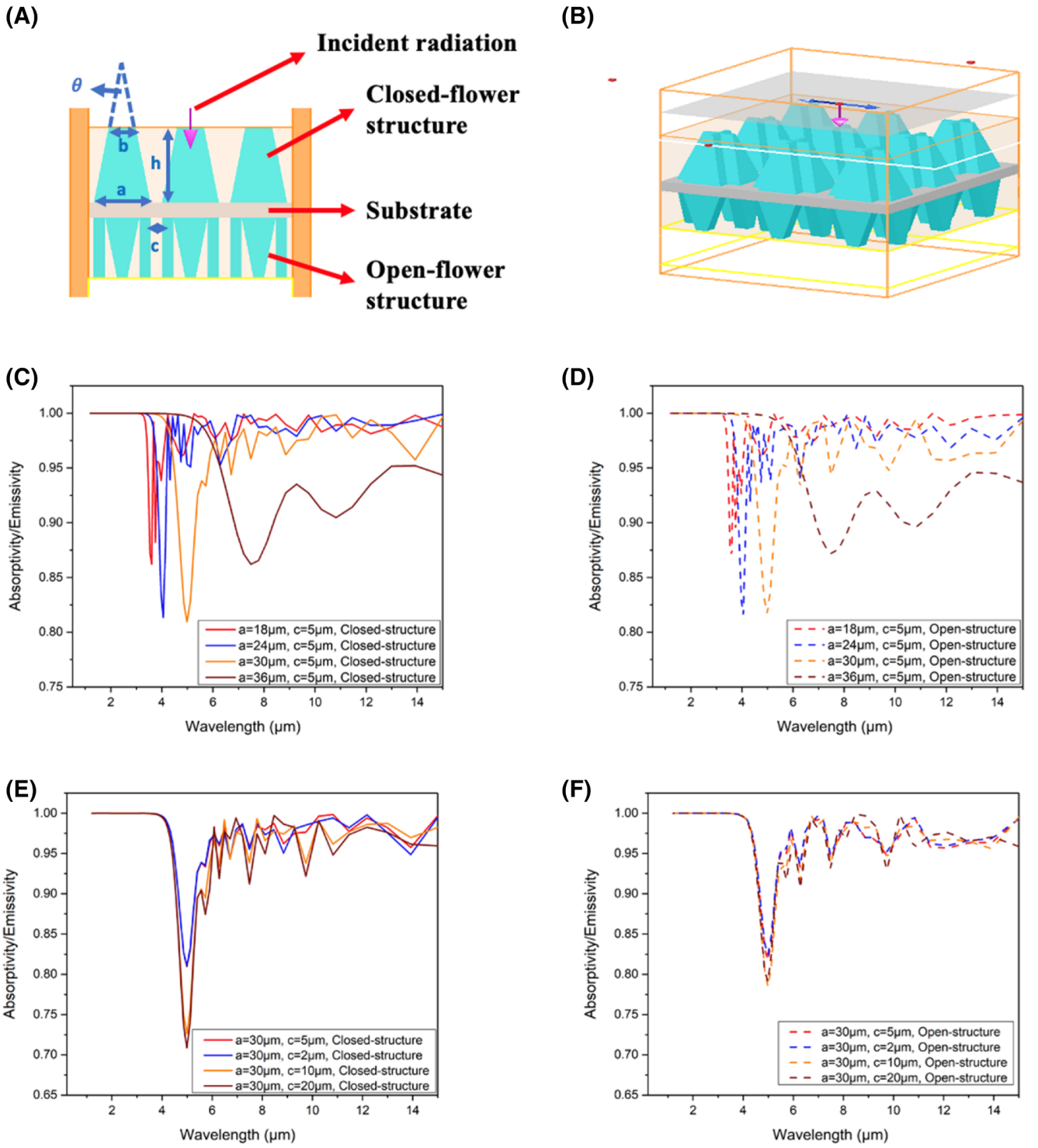

FIGURE 3 Simulation of emissivity of the EAM structures. (A), side-view of the designed structure. (B), the designed model in Lumerical FDTD simulation. (C, D), simulated absorption/emission spectra of different lateral size for closed-structure and open-structure, respectively. (E, F), simulated absorption/emission spectra of different gap distance for closed-structure and open-structure, respectively

the hydrogel but reduces the response capability to the environmental stimulus. On the contrary, it is hard to construct hydrogel using a low crosslinker concentration while the response to the stimulus is enhanced. Therefore, the balance between functionality and feasibility is an initial challenge. According to the literature,[24,25] the molar ratio of NIPAM and Mbis at 10:1 was a good trade-off. Besides the monomer and crosslinker, the photoresist also contains the photoinitiator (PI). Since the laser wavelength of the two-photon laser lithography is

780 nm, the absorption peak for the PI should be around 390 nm. Therefore, 2-hydroxy-4′-(2-hydroxyethoxy)-2-methylpropiophenone (Irgacure 2959) was selected as the PI in the photoresist. The PI was dissolved in the ethylene glycol (EG) and acetone first to ensure dispersion for polymerization.

Another challenge for fabricating the PNIPAM microstructures is to adjust the printing parameters to increase the printability.[26–28] Möller et al.[25] indicated that the pure NIPAM and Mbis photoresist is hard to print by two-photon polymerization due to the low energy delivery rate. Even if the scan speed was as low as 2000 μm/s and the laser power was as high as 80 mW, the printing process was still difficult, and the resolution was low. Here, one promising strategy to solve this problem is to cover the NIPAM resin with a commercialized IP-L 780 resin layer to increase power delivery.[29] These two kinds of resin are interpenetrated on a scale smaller than the wavelength of the light. The gelation diagram of each gel photoresist is shown in Figure 4. By introducing the compound photoresist of NIPAM, Mbis, PI, PNIPAM, and IP-L 780, the NIPAM resin can be polymerized under 10 000 μm/s scan speed and 30–40 mW power, respectively. The resolution can be at a 100 nm level. In the design, when the ambient temperature is higher than the critical temperature (T_c) of PNIPAM, the polymer shrinks and stiffens because of the hydrophobic property. The magnitude of this effect highly depends on the density of crosslinking during the polymerization process. With the higher crosslinking density of the polymer chains, the structure is more confined to its designed geometry and is harder to transform. In this case, the thermal response for the highly crosslinked area is weak. To achieve shape transformation between the open-flower and closed-flower structures, each triangular prism can be divided into two layers, as shown in Figure 2(A). The inner layer of the triangular prism indicated in yellow (lower crosslinking density) demonstrated a stronger shrinking than the outer layer shown in green (higher crosslinking density), which led to a pronounced bending towards the closed-flower structure when the temperature is higher than the critical temperature of PNIPAM.

The crosslinking density can be controlled by the exposure dose delivered to the curing region. A larger exposure dose results in a higher crosslinking density, while the lower exposure dose indicates a lower crosslinking density. To vary the local exposure dose during the fabrication process, the gradient of laser power can implement the exposure dose slope when the scan speed is constant. This method is called gray-tone lithography, which gradually changes the material properties by continuously varying the exposure dose during the fabrication process.[30] In this method, a highly localized control of the crosslinking density can be achieved, and, consequently, the thermal responsive structure was fabricated. The detailed printing parameters are stated in the method (section 6). Specifically, the green layers in Figure 1(A) were printed at 40 mW, and the yellow layers were printed at 30 mW, respectively. After that, the printed PNIPAM microstructures were transferred to acetone to remove the IP-L 780 resin, followed by DI water immersion. After development, the samples were kept in DI water to avoid drying of the formed hydrogel.

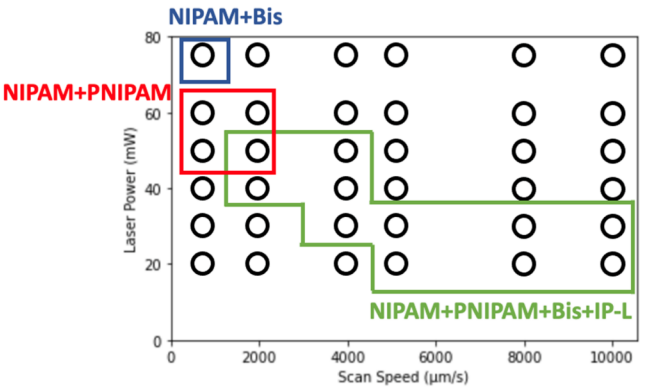

FIGURE 4 Gelation diagram of each gel photoresist. Different laser powers and scanning speeds ranging from 20 to 80 mW and 600 to 10 000 mm/s, respectively, were applied to gel photoresists composed of NIPAm + Bis with or without PNIPAm, and IP-L 780

4 | OPTICAL AND THERMAL PROPERTIES

To investigate the thermal response of the as-designed structure, as-printed samples were heated or cooled to the desired temperature controlled by a thermoelectric Peltier plate powered by Keithley 2400. According to the ambient temperature, the shape transformation was evaluated by the optical microscope (Figure 5(A)). When the ambient temperature is lower than T_c of PNIPAM (32°C), the as-printed structure exhibited the original printed shape, that is, open-flower form. As the ambient temperature went higher than T_c, PNIPAM transited from hydrophilic to hydrophobic, which resulted in the shrinkage in volume. Since the crosslink density of the outer layer (green layer) is higher than that of the inner layer for each prism, the transition of outer layers is not as sharp as that of the inner layers. Therefore, the open-flower structure was bent to the closed flower structure when the ambient temperature was 40°C. After the ambient temperature was decreased to room temperature, PNIPAM exhibited hydrophilic property again and tended to swell in water. The closed-flower structure was

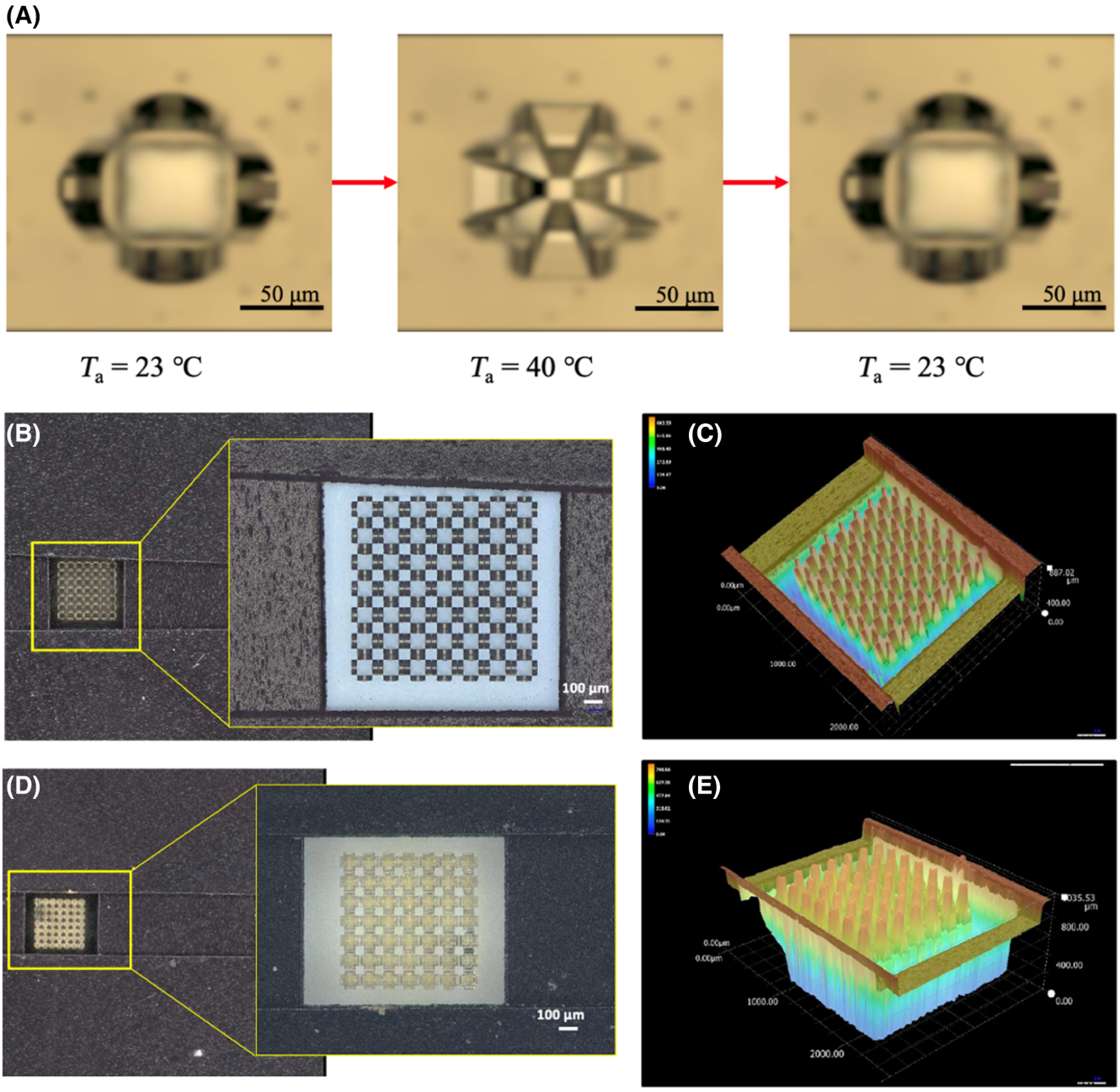

FIGURE 5 Environmentally adaptive micro-structure fabrication. (A) Temperature-induced transformation between open-flower structure and closed-flower structure. (B–C) Top view and 3D image of printed open-flower structure. (D–E) Top view and 3D image of printed closed-flower structure

re-open to the open-flower shape. This ability to change shape with temperature stimulus provides an excellent opportunity for the realization of EAM.

To experimentally verify the radiative cooling and heating performance of the designed responsive structure, we fabricated patterned structures on substrates for further measurements. Since it is very time-consuming to print deformable structures with a 63× lens (30 min for an open-flower form), we use a 25× lens to print non-deformable systems on a 1.5 × 1.5 mm scale to measure the emissivity of EAM. According to the numerical simulation results, the emissivity highly depends on the geometric parameter of the structure. In this case, four groups of samples for both closed-flower structure and open-flower structure were prepared for testing. The parameters of the system are listed in Table 1. In this design, the bottom lengths of the structure were ranged from 30 μm to 120 μm, the thickness of each triangular prism d is 1/3 of the bottom size a, the gap distance is a constant at 5 μm, and the height of the structure was

calculated based on the vertex angle of the pyramid structure. Figure 5((B)–(E)) shows the printed open-flower structure and closed-flower structure when $a = 90$ μm. Other printed samples for both open-flower structure and closed-flower structure are detailed in the Supplementary materials.

TABLE 1 Geometric parameters of the printed structure

Sample #	a (μm)	d (μm)	c (μm)	h (μm)	a/c
1	120	40	5	425	24
2	90	30	5	311	18
3	60	20	5	197	12
4	30	10	5	83	6

The next step is to investigate the radiative cooling and heating function of the designed EAM. The experimentally measured emissivity (absorptivity) spectra of the EAM were performed by UV–Vis–NIR spectroscopy in the range of 0.4–3 μm and Fourier-transform infrared (FTIR) spectroscopy in the field of 4–16 μm. The results are shown in Figure 6(A). The common radiative cooling emitter requires wide-band emissivity from wavelengths 8–13 μm with a high emission rate. For a single layer of the closed-flower structure ($a = 30$, 60, 90, and 120 μm), the peak emission rate is around 95% in the range of

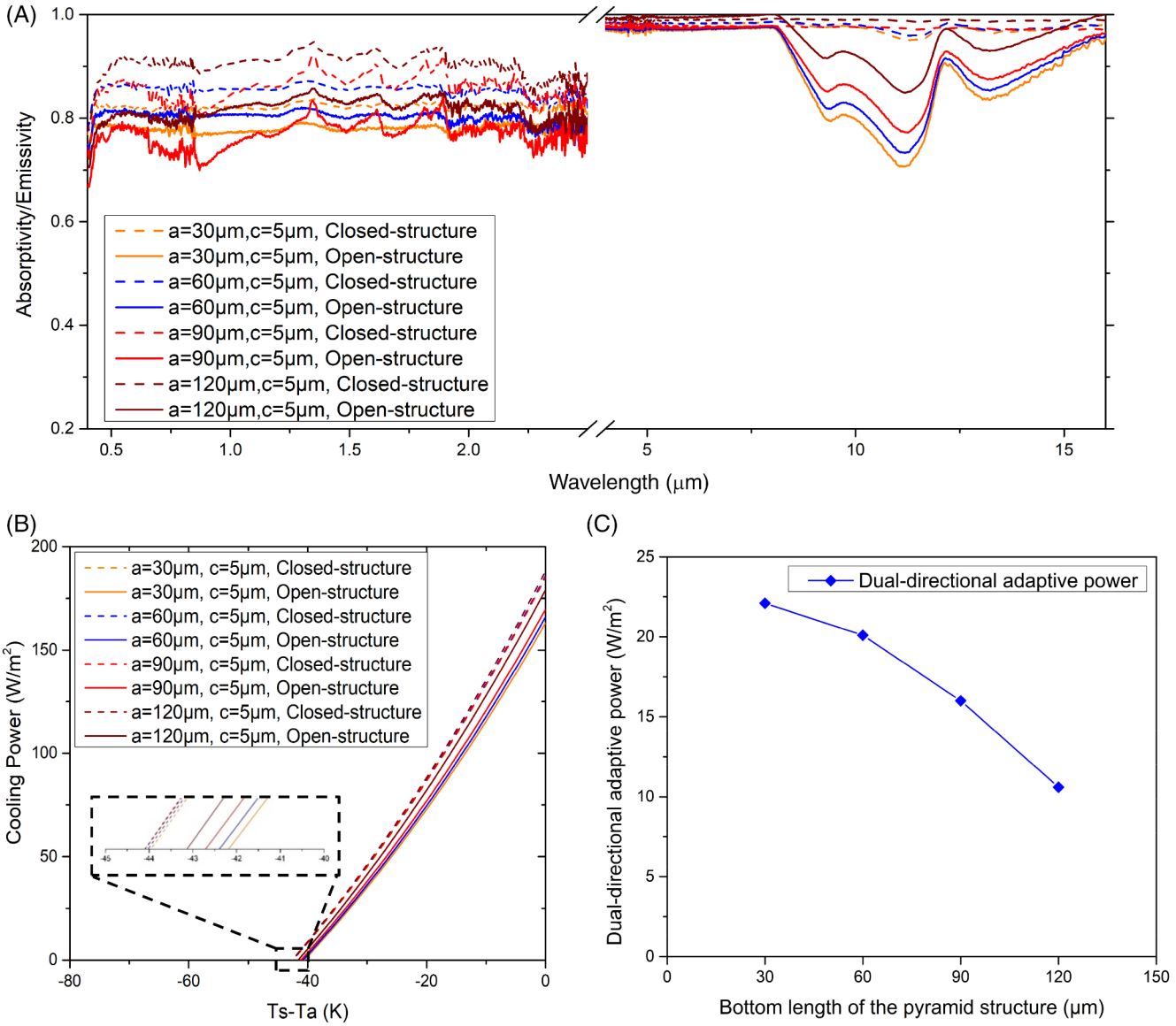

FIGURE 6 Optical properties of the EAM. (A) Measured emissivity (absorptivity) of the EAM for different bottom lengths of the pyramid structure. The wavelength ranged from 0.4 to 3 μm was measured by UV–vis–NIR and the wavelength ranged from 4 to 16 μm was measured by FTIR. (B) Calculated cooling power without the presence of nonradiative heat exchange for different bottom lengths of the pyramid structure. (C) Net cooling (heating) power of the designed EAM for different bottom lengths of the pyramid structure

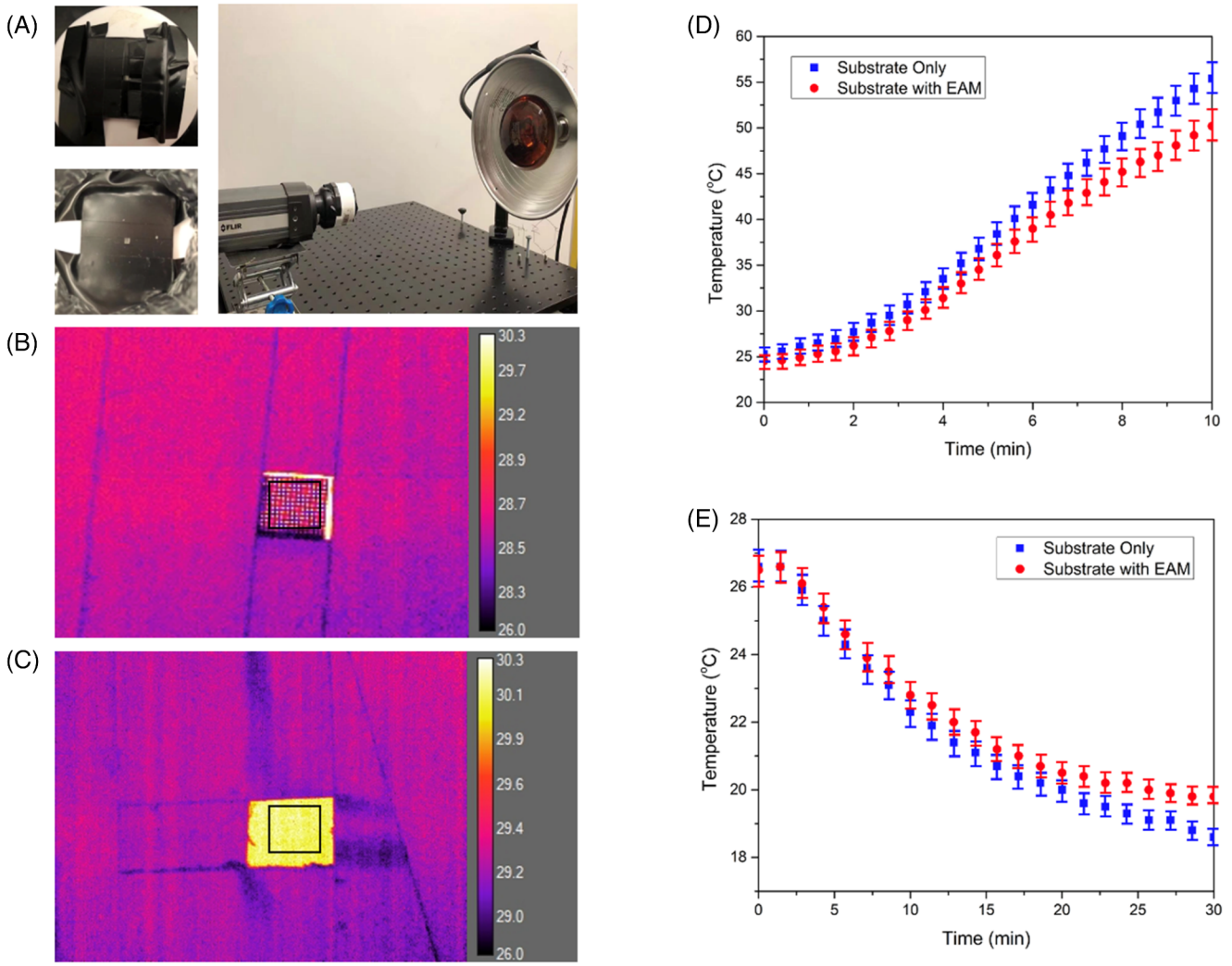

FIGURE 7 Thermal measurement of the EAM. (A) The cooling and warming test system. (B, C) The temperature distribution of the experimental group and the control group respectively. (D) Cooling effect of the experiment group (EAM on the substrate) and the control group (substrate only), respectively. (E) Heating effect of the experiment group (EAM on the substrate) and the control group (substrate only), respectively

atmospheric window. As the bottom length a increased, the peak emission rate became higher. But the difference is tiny. On the other hand, for a single layer of the open-flower structure (a = 30, 60, 90, and 120 μm), the emission rate decreased in the range of atmospheric window as the bottom length a increased. The lowest emission rate occurs on the 30-μm open-flower structure. The absorptivity dependence on geometrical parameters can be attributed to the bottom width and the gap ratio. If the ratio is smaller, which indicates the gap is more significant, it is easier for IR radiation to pass through the EAM, and the absorption rate is lower. To achieve both radiative cooling and heating by a double-layer structure, the difference of the emissivity between the open-flower and closed-flower structures is the most critical issue. The larger the difference will result in the better the radiative cooling and heating effect. As indicated in the Figure 6(A), the structure transition could lead to ∼35% difference between the emissivity in open flower and in closed flow states.

To evaluate the potential radiative cooling and heating effect of the EAM, the cooling power should be calculated. (Heating power is the opposite of cooling power. Therefore, we can calculate cooling power only.) Generally, the cooling power is subjected to the emitted radiative energy by the emitter and the absorbed atmospheric radiation by the structure. The detailed calculation steps are stated in the experiment section. Figure 6 (B) shows the cooling power for a single layer of the emitter, including the closed-flower structure and the open-flower structure. A positive value of cooling power can cool a chamber below the ambient temperature. When

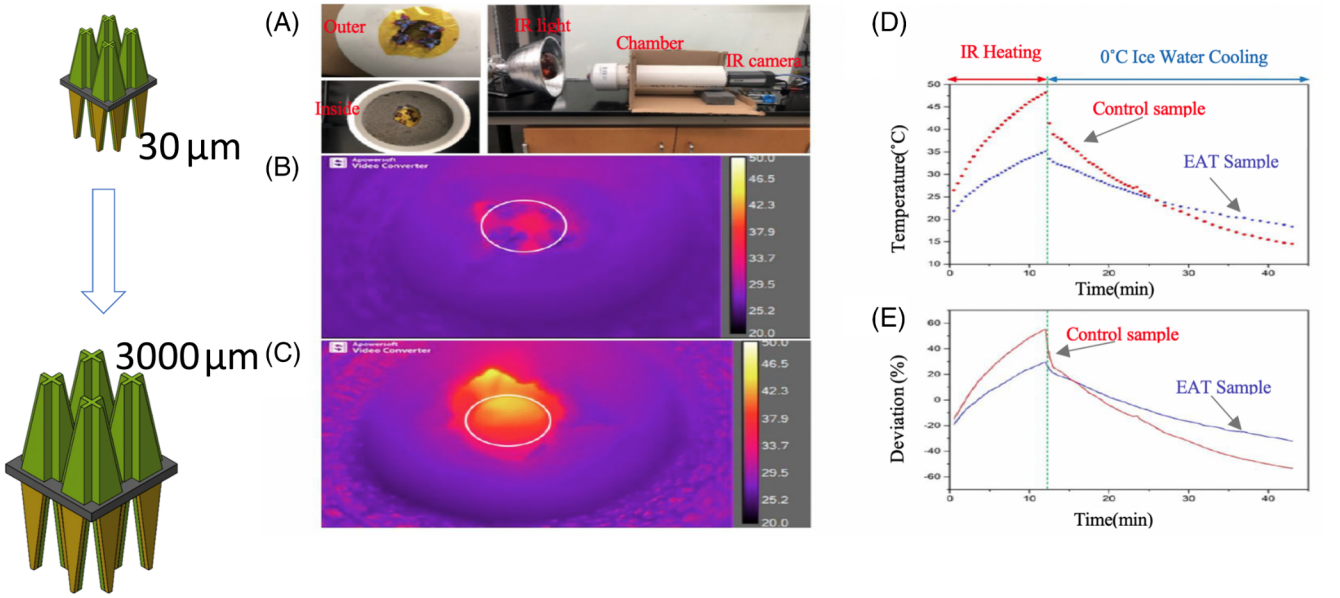

FIGURE 8 Thermal measurement of the scaled EAM (100× larger). (A) The cooling and warming test system. (B, C) the temperature distribution of the experimental group and the control group, respectively. (D) Cooling effect of the experiment group (EAM on the substrate) and the control group (substrate only), respectively. (E) Heating effect of the experiment group (EAM on the substrate) and the control group (substrate only), respectively

the cooling power is 0, the value of $(T_s - T_a)$ indicates the temperature difference that can be achieved between the ambient environment and the covered chamber. On the other hand, when $(T_s - T_a) = 0$, the net cooling power for the 30-μm closed-flower structure is as high as 185 W/m^2. Similarly, when outside temperature is cold, we will use $(T_s - T_a)$ as an indicator of the temperature difference, and the net warming power could also reach as high as 185 W/m^2.

The traditional evaluation criteria work for radiative cooling power only, which is not sufficient for dual-functional membranes. In this case, a novel strategy to evaluate the performance of dual-functional membranes should be created. The dual-functional membranes exhibit both radiative cooling and heating functions. For a double-layer structure, the closed-flower structure towards outside, and the open-flower structure towards insides, achieves radiative cooling when the ambient temperature is high. The cooling power can be calculated by the reflected ambient IR radiation minus the conserved heat from the inside. When the ambient temperature is low, the inside emitter changes to the closed-flower structure, and the outside emitter changes to the open-flower structure. The heating power should be considered as the difference between the absorbed ambient IR radiation and the inside heat emission. Therefore, the absorptivity difference for the inside and outside structure should be applied to the Equations (1)–(5) shown in the Section 6, that is

$$P_{\text{dual-directional adaptive power}} = |P_{\text{outside}} - P_{\text{inside}}| = |f(e_s(\text{outside}) - e_s(\text{inside}))|$$

where the e_s(outside) and e_s(inside) refer to the emissivity of the outside layer and the inside layer, respectively. At this moment, the dual-directional adaptive power can be calculated by the difference of the absorptivity for the closed-flower and open-flower structures based on the results in Figure 6(A). The dual-directional adaptive powers are shown in Figure 6(C). The EAM can exhibit "smart" radiative cooling and heating power at 22 W/m^2 when the 30-μm structures were applied.

To measure the radiative cooling and heating effect of the EAM, a homemade thermographic camera system was set up. The testing system consists of an IR camera, one sample holder for the double-layer EAM, and the ambient temperature control system (Figure 7(A)). A 1-inch length hole was punched on an isothermal chamber to anchor the EAM sample. The EAM sample was fabricated by the 25× lens to print non-deformable structures on a 1.5 × 1.5 mm square. Due to the resolution of the IR camera being 50 μm, the structure size for the testing was the 60-um closed-flower and open-flower structures. For the experiment group, the outside layer of the EAM sample is covered by the closed-flower structure, and the inside layer is covered by the open-flower structure. As the control group, a clean glass substrate was set on the sample position. The hot environment was created by a 250 W IR heater, and the cold climate was generated by a box of ice water mixture.

Figure 7((B)–(C)) shows the temperature distribution captured by the IR camera for the same heating duration (10 min) and the same cooling duration (30 min) for the experiment group and control group, respectively. The average temperature of all the pixels in the black square in Figure 5((B)–(C)) was calculated over time and plotted in Figure 7((D)–(E)). The movie was captured by the IR camera in the Supplementary materials. As shown in Figure 7 ((B)–(C)), the heating and cooling processes of the experimental group are slow than the control group, which indicates improved cooling and heating performance. The calculated dual-directional adaptive of the printed sample was 45 μW on the 1.5 × 1.5 mm square.

To investigate the scalability of the designed EAM, centimeter-scaled membranes (2.54 × 2.54 cm) were printed using direct ink writing. Specifically, the flower size was changed from previous 30 to 3000 μm in order to reduce the printing time, as shown in Figure 8. The cooling and warming functions were also tested by self-designed setup (Figure 8(A)). A 1-inch diameter hole was punched on an isothermal chamber. For the experiment group the outside layer of the hole is covered by the top-layer structure and the inside layer is covered by the bottom-layer structure for the experimental group. As the control group, both sides of the hole were covered by Kapton film only. Figure 8((B)–(C)) show the temperature distribution captured by IR camera for the same heating duration (5 min). The average temperature of all the pixels in the white circle in Figure 8((B)–(C)) was calculated over the time period and plotted in Figure 8(D). As shown in the figure, the heating process and the cooling process of the experimental group are slower than the control group which indicates improved cooling and warming performance. The deviation of each group compared to their own average temperature indicates the temperature fluctuation of the experimental group is lower than that of the control group, as shown in Figure 8(E). The centimeter-scaled structure proves the confidence of manufacturing scalability and the feasibility for building cooling and warming applications.

5 | CONCLUSIONS

In summary, we have introduced PNIPAM-based environmental adaptive 3D microstructures by two-photon polymerization. The in-gel laser writing approach was applied to increase the accuracy and printability of PNIPAM microstructures. Thus, a thermal responsive polymer flower structure was designed and fabricated, and it could undergo a transition between open-flower and close-flower states at 32°C within 1 min, resulting in ∼35% difference between the emissivity in open flower and in close flower states. As a result, the power difference between inner layer and outer layer was as high as 22 W/m^2 and is a function of pyramid bottom size. This technology has the potential to reduce the energy consumption of heating, ventilation, and air conditioning (HVAC) systems for both buildings and electrical vehicles (EVs) enabling improved energy and environmental sustainability.

6 | METHODS

6.1 | Materials

N-isopropylacrylamide (Sigma-Aldrich, >97%), N,N′-methylenebis (acrylamide) (Sigma-Aldrich, >99%), 2-hydroxy-4′-(2-hydroxyethoxy)-2-methylpropiophenone (Irgacure 2959) (Sigma-Aldrich, >98%), Rhodamine B Tetraethylrhodamine (Sigma-Aldrich, >95%), Methylene Blue 3,7-bis(Dimethylamino)phenazathionium chloride (sigma Aldrich, >82%), 3-(trimethoxysilyl)propyl methacrylate (Sigma-Aldrich, >97%), ethylene glycol (Macron Fine Chemicals, >99%), acetone (Macron Fine Chemicals, >99.5%), isopropanol (Macron Fine Chemicals, >99.5%), IP-L 780 Resin (Nanoscribe GmbH), IP-S Resion (Nanoscribe GmbH). All chemicals and solvents were used as received without further purification.

6.2 | NIPAM resist synthesis

A 10 mg Irgacure 2959 was dissolved in 500 μL ethylene glycol and 500 μL acetone mixture. Then 400 mg N-isopropylacrylamide (NIPAM) and 40 mg N,N′-methylenebis(acrylamide) (Mbis) were added to the solutions and incubated overnight.

6.3 | Pretreatment of substrates

Since the microstructure can only be printed on the 170-μm-thick coverslips, the coverslips were successively immersed into acetone, ethanol, and DI water by sonication, each for 15 min. Then the coverslips were treated with UV-ozone for 30 min to make the surface hydrophilic. To increase the adhesion of the microstructures to the coverslips, the coverslips were treated by 3-(trimethoxysilyl)propyl methacrylate (1 mM in toluene) for 1 h. After being washed with acetone and DI water, the coverslips were dried under nitrogen.

6.4 | Fabrication of 3D microstructures

A commercial Direct Laser Writing setup (Nanoscribe Photonics GT2 high-resolution 3D printer, Nanoscribe

GmbH) with 25×, NA = 0.8 and 63×, NA = 1.4 oil immersion objective was used for fabrication. To fabricate the thermal responsive structure formed by PNIPAM, as prepared NIPAM resist was drop cast onto the pretreated coverslips. Then add a drop of IPL-780 on the top of the NIPAM resist. The thermal responsive structure was achieved with a laser power at the inner focal plane of 35 mW and the outer focal plane with 40 mW, respectively. The scan speed was set constantly at 10 mm/s. After writing, the structures were rinsed with acetone and subsequently transferred into DI water for further development. No post-curing treatment was applied to the structure.

6.5 | Characterization

The optical microscope (Nikon Eclipse LV150N) was used to observe the morphology of the printed structure. To analyze the thermal response of the samples to changes in temperature, the thermoelectric Peltier plate was power by Keithley 2400, and the temperature was measured by TC-2000 with thermal couples. The 3D-structure of the samples was measured by Keyence VHX-7000. Absorbance/Emissivity characterization was carried out by the ATR-FTIR spectrometer (Bruker Alpha-Platinum), and UV–Vis–NIR spectrometer (Hitachi U-4100) for the wavelength range at 2 –20 μm and 0.2–2 μm, respectively. The IR images and videos were recorded by the FLIR IR camera (48001-1001, −20°C to 350°C) with a 2× lens (T197214, IFOV 50 μm, WD = 33 mm).

6.6 | Radiative cooling power calculation

The cooling power calculation is followed the method published by Min Gu et al.[14] Briefly, the net cooling power of the emitter can be defined as:

$$P_{\text{net}} = P_{\text{r}} - P_{\text{a}} \tag{1}$$

Here, P_{r} is the power radiated by the emitter, and P_{a} is the incident atmospheric radiation absorbed by the emitter.

First,

$$P_{\text{r}} = \int_0^{\frac{\pi}{2}} \pi sin2\theta d\theta \int_0^{\infty} U_{\text{B}}(T_{\text{s}},\lambda) e_{\text{s}}(\lambda,\theta) d\lambda \tag{2}$$

where

$$U_{\text{B}}(T,\lambda) = \frac{2hc^2}{\lambda^5} \frac{1}{e^{hc/\lambda k_B T} - 1} \tag{3}$$

is the spectral radiance of a blackbody defined by Planck's law at temperature T where h is the Planck constant, kB is the Boltzmann constant, c is the speed of light, λ is the wavelength, and T_{s} is the temperature of the emitter.

The factor $e_{\text{s}}(\lambda,\theta)$ in Equation (2) is the emissivity of the EAM, which is measured by the UV–Vis–NIR spectrometer and ATR-FTIR spectrometer according to Kirchhoff's Law.

Similarly, the absorbed incident radiation P_a can be calculated by:

$$P_{\text{a}} = \int_0^{\frac{\pi}{2}} \pi sin2\theta d\theta \int_0^{\infty} U_{\text{B}}(T_{\text{a}},\lambda) e_{\text{s}}(\lambda,\theta) e_{\text{a}}(\lambda,\theta) d\lambda \tag{4}$$

The angle-dependent emissivity factor $e_{\text{a}}(\lambda,\theta)$ is given by:

$$e_{\text{a}}(\lambda,\theta) = 1 - t(\lambda)^{1/cos\theta} \tag{5}$$

where $t(\lambda)$ is the atmospheric transmittance in the zenith direction. The data of $e_{\text{a}}(\lambda,\theta)$ can be found from Gemini Observatory.[20] T_{a} is the ambient temperature, which is considerate to be 300 K. The calculation was performed using a Python program and database (Pandas).

6.7 | Numerical simulation

The numerical simulations were carried out using the finite element (FE) method, and the finite-difference time domain (FDTD) approaches based on Maxwell's Equations and heat transfer model. Since the radiative cooling performance highly depends on the geometrical structure of the light reflection surface, several dimensional factors of the closed-flower structure needed to be studied. The overall emissivity of the membranes were calculated with different dimensional factors, including the height, the layer thickness, and the gap distance of linear structures to illustrate the role of different factors. The equations were solved by Lumerical FDTD Solutions.

ACKNOWLEDGMENT

We are grateful to the financial supports from State of Texas, National Science Foundation, and Texas A&MT3 grant support.

AUTHOR CONTRIBUTIONS

Yuchen Liu: Conceptualization (equal); data curation (equal); formal analysis (equal); investigation (equal); methodology (equal); writing – original draft (lead); writing – review and editing (equal). **Ruochen Liu:** Data curation (equal); formal analysis (equal); investigation (equal); methodology (equal); writing – review and editing (equal). **JJingjing Qiu:** Project administration (equal); resources (equal); supervision (equal); writing – review and editing (equal). **Shiren Wang:** Conceptualization (lead); funding acquisition (equal); project administration (equal); resources (equal); software (equal); supervision (equal); writing – review and editing (equal).

CONFLICT OF INTEREST

The authors declare no competing interests.

DATA AVAILABILITY STATEMENT

The data that supports the findings of this study are available in the supplementary material of this article.

ORCID

Shiren Wang https://orcid.org/0000-0003-4516-3025

REFERENCES

[1] D. Roy, W. L. Brooks, B. S. Sumerlin, *Chem. Soc. Rev.* **2013**, *42*(17), 7214.
[2] R. Geryak, V. V. Tsukruk, *Soft Matter* **2014**, *10*(9), 1246.
[3] D. Sun, R. T. Pinker, M. Kafatos, *Geophys. Res. Lett.* **2006**, *33*(5), L05705.
[4] M. Qu, J. Wan, X. Hao, *Weather Clim. Extr.* **2014**, *4*, 86.
[5] B. Czapla, A. Srinivasan, Q. Yin, A. Narayanaswamy, In potential for passive radiative cooling by PDMS selective emitters, ASME 2017 Heat Transfer Summer Conference, American Society of Mechanical Engineers Digital Collection; **2017**.
[6] M. Hu, G. Pei, Q. Wang, J. Li, Y. Wang, J. Ji, *Appl. Energy* **2016**, *179*, 899.
[7] A. P. Raman, M. A. Anoma, L. Zhu, E. Rephaeli, S. Fan, *Nature* **2014**, *515*(7528), 540.
[8] P.-C. Hsu, A. Y. Song, P. B. Catrysse, C. Liu, Y. Peng, J. Xie, S. Fan, Y. Cui, *Science* **2016**, *353*(6303), 1019.
[9] H. Bao, C. Yan, B. Wang, X. Fang, C. Zhao, X. Ruan, *Sol. Energy Mater. Sol. Cells* **2017**, *168*, 78.
[10] Y. Zhai, Y. Ma, S. N. David, D. Zhao, R. Lou, G. Tan, R. Yang, X. Yin, *Science* **2017**, *355*(6329), 1062.
[11] L. Zhu, A. P. Raman, S. Fan, *Proc. Natl. Acad. Sci.* **2015**, *112*(40), 12282.
[12] Y. Lu, Z. Chen, L. Ai, X. Zhang, J. Zhang, J. Li, W. Wang, R. Tan, N. Dai, W. Song, *Solar Rrl.* **2017**, *1*(10), 1700084.
[13] D. Wu, C. Liu, Z. Xu, Y. Liu, Z. Yu, L. Yu, L. Chen, R. Li, R. Ma, H. Ye, *Mater. Des.* **2018**, *139*, 104.
[14] M. M. Hossain, B. Jia, M. Gu, *Adv. Opt. Mater.* **2015**, *3*(8), 1047.
[15] X. A. Zhang, S. Yu, B. Xu, M. Li, Z. Peng, Y. Wang, S. Deng, X. Wu, Z. Wu, M. Ouyang, *Science* **2019**, *363*(6427), 619.
[16] X. Li, B. Sun, C. Sui, A. Nandi, H. Fang, Y. Peng, G. Tan, P.-C. Hsu, *Nat. Commun.* **2020**, *11*(1), 1.
[17] S. Maruo, O. Nakamura, S. Kawata, *Opt. Lett.* **1997**, *22*(2), 132.
[18] H. Ko, A. Javey, *Acc. Chem. Res.* **2017**, *50*(4), 691.
[19] T.-Y. Wu, A. B. Zrimsek, S. V. Bykov, R. S. Jakubek, S. A. Asher, *J. Phys. Chem. B.* **2018**, *122*(11), 3008.
[20] Atmospheric transmittance. https://www.gemini.edu/observing/telescopes-and-sites/sites#MK%20thermal-infrared%20extinction.
[21] AM 1.5 solarspectrum. https://www.nrel.gov/grid/solar-resource/spectra-am1.5.html.
[22] S.-P. Lv, S.-H. Liu, Y.-B. Zhao, *Mater. Technol.* **2005**, *20*(4), 211.
[23] M. Li, B. Bresson, F. Cousin, C. Fretigny, Y. Tran, *Langmuir* **2015**, *31*(42), 11516.
[24] M. Hippler, E. Blasco, J. Qu, M. Tanaka, C. Barner-Kowollik, M. Wegener, M. Bastmeyer, *Nat. Commun.* **2019**, *10*(1), 1.
[25] A. Nishiguchi, H. Zhang, S. R. Schweizerhof, M. F. Schulte, A. Mourran, M. Möller, *ACS Appl. Mater. Interfaces* **2020**, *12*(10), 12176.
[26] M. Champeau, D. A. Heinze, T. N. Viana, E. R. de Souza, A. C. Chinellato, S. Titotto, *Adv. Funct. Mater.* **2020**, *30*(31), 1910606.
[27] X. Kuang, D. J. Roach, J. Wu, C. M. Hamel, Z. Ding, T. Wang, M. L. Dunn, H. J. Qi, *Adv. Funct. Mater.* **2019**, *29*(2), 1805290.
[28] H. Y. Jeong, E. Lee, S.-C. An, Y. Lim, Y. C. Jun, *NANO* **2020**, *9*(5), 1139.
[29] A. Nishiguchi, A. Mourran, H. Zhang, M. Möller, *Adv. Sci.* **2018**, *5*(1), 1700038.
[30] J. Qu, M. Kadic, A. Naber, M. Wegener, *Sci. Rep.* **2017**, *7*, 40643.

SUPPORTING INFORMATION

Additional supporting information may be found in the online version of the article at the publisher's website.

How to cite this article: Y. Liu, R. Liu, J. Qiu, S. Wang, *J. Adv. Manuf. Process.* **2022**, *4*(2), e10107. https://doi.org/10.1002/amp2.10107